

# All-Optical Universal Control of Hyperfine Qudits in Trapped Neutral Atoms

Johannes K. Krondorfer,<sup>1,\*</sup> Matthias Diez,<sup>1,2</sup> Andreas Kruckenhauser,<sup>3</sup> and Andreas W. Hauser<sup>1,†</sup>

<sup>1</sup>*Institute of Experimental Physics, Graz University of Technology, Petersgasse 16, 8010 Graz, Austria*

<sup>2</sup>*Institute of Physics, University of Graz, Universitätsplatz 5, 8010 Graz, Austria*

<sup>3</sup>*PlanQC GmbH, 85748 Garching, Germany*

(Dated: May 12, 2026)

Quantum systems with more than two levels – so-called *qudits* – offer increased computational density and reduced circuit complexity compared to qubit-based architectures, but achieving universal and scalable control remains challenging. We propose an all-optical scheme for universal qudit control in trapped neutral atoms in moderate to high magnetic fields, focusing on the fermionic isotope  $^{173}\text{Yb}$  ( $I = 5/2$ ). The strong hyperfine interaction in the  $^3P_1$  manifold enables fast and selective Raman transitions between nuclear-spin states in the  $^1S_0$  ground-state manifold using a single linearly polarized laser. For each neighboring transition in the qudit manifold, we identify a magic polarization angle that enables coherent, state-selective control while suppressing off-resonant excitations, with operation frequencies exceeding 100 kHz. Combined with phase-shift operations, this provides universal control of the full single-qudit space. We further discuss compatible two-qudit gates based on the Rydberg blockade mechanism, completing a universal gate set, and analyze state-selective readout schemes compatible with the proposed protocol. Our results identify  $^{173}\text{Yb}$  as a promising platform for high-fidelity, all-optical qudit-based quantum information processing.

## I. INTRODUCTION

Quantum information processing relies on the ability to manipulate quantum states coherently. Most architectures encode quantum information in binary form using qubits, two-level quantum systems that serve as the basic unit of computation.

However, quantum computation with qudits, i.e., multi-level quantum systems, offers several advantages over binary qubit encodings. These include an increased computational density, enabling a more compact representation of quantum states, as well as a reduction in circuit complexity and entangling gate count through the compression of multi-qubit operations into fewer multi-level gates [1–3]. In addition, qudits provide a natural framework for the efficient encoding of local Hilbert spaces and symmetries that arise in quantum simulation, such as non-Abelian gauge degrees of freedom [4, 5]. In this context, recent experiments have demonstrated programmable qudit processors and simulations of lattice gauge theories [6, 7]. Furthermore, higher-dimensional systems enable more compact logical encodings and can improve fault-tolerant thresholds in quantum error correction [8].

At the same time, these advantages come at the cost of increased control complexity. In contrast to qubit architectures, where universal control can be implemented using a small set of well-characterized single- and two-qubit gates, qudit systems require selective and coherent coupling between multiple levels, which leads to a higher susceptibility to unwanted couplings and leakage processes [9–12]. Nevertheless, recent work has demonstrated that, with careful engineering of driving fields

and level structures, high-fidelity and selective control of multi-level systems is achievable [6, 13, 14].

These considerations motivate the exploration of physical platforms that naturally support multi-level encoding while enabling precise and scalable control of their internal states. Qudit-based quantum information processing has been explored in a variety of systems, including superconducting circuits [15, 16], trapped ions [6, 7, 17], and neutral atoms [10, 11, 13].

Trapped neutral atoms, in particular, are among the most promising candidates for scalable quantum computing. Specifically, alkaline-earth and alkaline-earth-like atoms such as strontium and ytterbium are attractive due to their well-understood fine and hyperfine structure, narrow optical transitions, and the ability to precisely control their interactions with external fields [18–20]. For qubit-based applications, the nuclear spin-1/2 isotope  $^{171}\text{Yb}$  has been widely adopted due to its versatile optical-metastable-ground-state (OMG) architecture [21, 22], where high-fidelity qubit gates [23–25], erasure conversion [26], and midcircuit measurements [21, 27, 28] have been demonstrated. These demonstrations highlight the maturity of optical control in ytterbium-based neutral-atom platforms, with single-qubit Rabi frequencies up to  $\sim 300$  kHz [23] and even  $\sim 1.77$  MHz [24], as well as microsecond-timescale Rydberg-mediated CZ gates [25]. However, the nuclear spin-1/2 isotope  $^{171}\text{Yb}$  only provides two hyperfine ground states. Hyperfine qudit encoding therefore requires isotopes with nuclear spin  $I > 1/2$ , whose ground-state nuclear-spin manifold naturally provides multiple long-lived internal states.

At the same time,  $^{87}\text{Sr}$  ( $I = 9/2$ ) has emerged as an important alkaline-earth platform for nuclear-spin qubits and qudits. Nuclear-spin qubits in tweezer arrays have been assembled and coherently controlled with long coherence times and Rabi frequencies up to the kHz regime [29]. Optical nuclear electric resonance (ONER)

\* johannes.krondorfer@gmail.com

† andreas.w.hauser@gmail.com

has been proposed as a complementary optical route to nuclear-spin control in high magnetic fields, with predicted Rabi frequencies up to  $\sim 20$  kHz [30–32]. The large nuclear spin of  $^{87}\text{Sr}$  further makes it a natural qudit platform. Qudit-control schemes based on magnetic radio-frequency fields and differential Stark shifts have been proposed [9, 10], and coherent control of the four lowest nuclear-spin levels has been demonstrated experimentally [13]. In addition, fully optical control of the complete ground-state manifold at high magnetic fields using ONER has been suggested [11].

The success of fast optical control in  $^{171}\text{Yb}$  and qudit studies in  $^{87}\text{Sr}$  motivates the exploration of  $^{173}\text{Yb}$  ( $I = 5/2$ ) as a native ytterbium qudit platform. This isotope combines a multi-level nuclear-spin ground-state manifold with large hyperfine splittings in the relevant excited states, which enhances level separation and facilitates spectrally selective Raman coupling. Although  $^{173}\text{Yb}$  has been studied in a variety of contexts, including  $\text{SU}(d)$  magnetism [33–35] and precision spectroscopy [36–38], it remains comparatively unexplored for quantum information processing and has only recently begun to attract attention in this direction [39].

In this work, we propose a scheme for all-optical universal qudit control in neutral  $^{173}\text{Yb}$  atoms. The scheme combines universal single-qudit control, generated by state-selective neighboring transitions and phase shifts, with an entangling two-qudit gate based on Rydberg blockade interactions. We further discuss compatible state-selective readout schemes, thereby completing the basic set of ingredients required for all-optical qudit operation. The following section provides a schematic outline of the protocol before we develop the Hamiltonian description and analyze its performance. Our results identify  $^{173}\text{Yb}$  as a promising platform for rapid and robust all-optical hyperfine-qudit control.

## II. ALL-OPTICAL QUDIT CONTROL

In this section, we discuss the scheme for all-optical universal qudit control in neutral  $^{173}\text{Yb}$  atoms, as illustrated in Fig. 1(a). Such control requires universal single-qudit operations together with an entangling two-qudit gate [40]. We consider the nuclear-spin manifold of the  $^1S_0$  ground state of  $^{173}\text{Yb}$ , which provides a six-dimensional qudit; the colors in Fig. 1(a) label the corresponding ground-state levels and operations used throughout the manuscript. An external magnetic field  $\mathbf{B} = B\hat{e}_z$  defines the quantization axis and lifts the degeneracy of the nuclear-spin states. A corresponding Breit–Rabi diagram is displayed in Fig. 1(b), illustrating the magnetic-field-dependent level structure of the relevant  $^3P_1$  excited-state manifold, with the  $^1S_0$  ground-state manifold shown in the inset.

The single-qudit control scheme uses off-resonant coupling to the  $^3P_1$  manifold with a single, linearly polarized laser. The laser is detuned from selected excited-

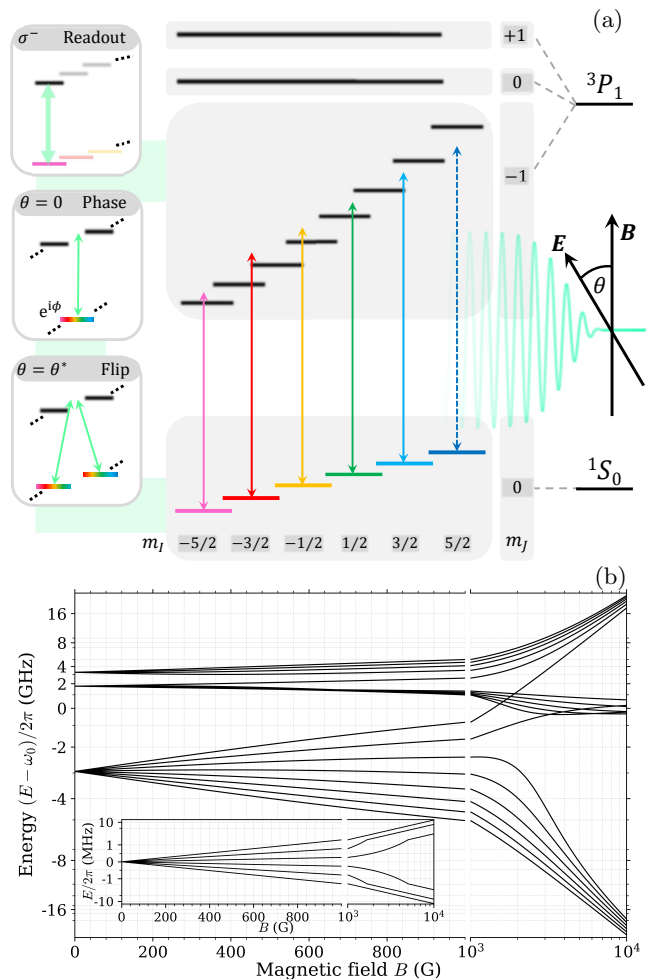


FIG. 1: Overview of the proposed control scheme and relevant level structure. (a) Schematic of the  $^{173}\text{Yb}$  nuclear-spin qudit in the  $^1S_0$  ground-state manifold. Colors label the ground-state levels and define the nearest-neighbor transition colors used throughout the manuscript. A linearly polarized laser field  $\mathbf{E}$  at angle  $\theta$  with respect to the magnetic field  $\mathbf{B}$  couples the ground-state manifold to selected states in the  $^3P_1$  manifold, generating flip operations, phase shifts, and state-selective readout as indicated schematically. (b) Breit–Rabi diagram of the relevant  $^3P_1$  level structure, with the  $^1S_0$  ground-state manifold shown in the inset. The energy axes are scaled to enhance visibility of the relevant states.

state levels such that these states are only virtually populated, but induce state-dependent light shifts and effective couplings within the ground-state manifold. This selectivity relies on the interplay between hyperfine interaction and magnetic field: the hyperfine interaction admixes nuclear-spin components in the excited states, while the magnetic field provides sufficient level spacing to keep unwanted couplings off-resonant. As a result, the light shifts depend on  $m_I$  and can compensate the Zeeman splitting between neighboring ground states, en-

abling resonant Raman transitions.

Two types of single-qudit operations can be realized by adjusting the polarization angle  $\theta$  between the magnetic field and the laser field. By setting the polarization to a transition-dependent *magic angle*  $\theta = \theta^*$ , resonant Raman transitions between neighboring states can be driven (“flip” operations, see Sec. IV A). For  $\theta = 0$ , ground-state transitions are prohibited, while state-dependent light shifts induce relative phase accumulation (“phase” operations, see Sec. IV B). Together, these operations generate universal control of the full single-qudit manifold, with achievable operation frequencies exceeding 100 kHz.

Entangling two-qudit gates can be implemented using Rydberg-mediated interactions, which are most robust when restricted to stretched states, as discussed in Sec. V. In particular, stretched ground states can be coupled via stretched Rydberg states in the  $6sns\ ^3S_1$ ,  $F = 7/2$  series, using an excitation structure compatible with recently demonstrated fast Rydberg gates in  $^{171}\text{Yb}$ . Extending such gates to the full qudit manifold is challenging because of the limited experimental data for  $^{173}\text{Yb}$  Rydberg states and the theoretical intricacies of modeling their level structure in moderate to high magnetic fields. We therefore focus on stretched-state implementations for entangling operations, while single-qudit control remains fully universal within the ground-state manifold.

Using the same stretched-state structure, state-selective readout can be achieved via optical fluorescence cycling, enabling high-fidelity detection by population mapping onto a stretched state; see Sec. VI. Either the narrow  $^3P_1$  transition or the broad  $^1P_1$  transition can be used, providing complementary regimes: the  $^3P_1$  transition enables high-contrast readout with lower scattering rates, while the  $^1P_1$  transition enables faster readout at reduced contrast.

### III. HAMILTONIAN DESCRIPTION AND EFFECTIVE MODEL

#### A. Atomic Structure and full Hamiltonian

Due to the favorable hyperfine structure, we concentrate on the  $(6s^2)\ ^1S_0 \rightarrow (6s6p)\ ^3P_1$  transition in  $^{173}\text{Yb}$  to achieve nuclear spin control in the ground state via single-beam Raman transitions, employing the principle outlined in Fig. 1. Note, however, that this approach can in principle be applied to other alkaline-earth-like atoms as well, while the large hyperfine splitting of  $^{173}\text{Yb}$  in the  $^3P_1$  manifold is particularly favorable for achieving selective coupling.

For our theoretical investigation, we consider the Hamiltonian of a  $^{173}\text{Yb}$  atom in an external constant magnetic field  $\mathbf{B}$  in positive  $z$ -direction, and a laser field with intensity  $\mathcal{I}$ , giving rise to a maximal electronic Rabi frequency  $\Omega_E$ , and a polarization angle  $\theta$ , with respect to the  $z$ -axis. This gives rise to the total Hamiltonian of the

system

$$H = H'_E(\Delta) + H_Z(\mathbf{B}) + H_{\text{HF}} + H_{\text{AF}}(\Omega_E, \theta), \quad (1)$$

with the electronic Hamiltonian in the rotating frame  $H'_E = -\Delta|{}^3P_1\rangle\langle{}^3P_1|$ , with  $\Delta = \omega_0 - \omega$ , where  $\omega_0$  is the central transition frequency of the  $(6s^2)\ ^1S_0 \rightarrow (6s6p)\ ^3P_1$  transition corresponding to 556 nm [24, 41], and  $\omega$  is the frequency of the laser field. Note that we set  $\hbar = 1$  throughout the manuscript. Additionally, we consider a decay from the  $^3P_1$  state to the  $^1S_0$  ground state with a decay rate of  $\Gamma = 2\pi \times 183$  kHz.[24, 41]

The Zeeman Hamiltonian  $H_Z$  and the hyperfine Hamiltonian  $H_{\text{HF}}$  are given by

$$H_Z(\mathbf{B}) = \left( g_J \mu_B \hat{\mathbf{J}} - g_I \mu_N \hat{\mathbf{I}} \right) \cdot \mathbf{B}$$

$$H_{\text{HF}} = A \hat{\mathbf{I}} \cdot \hat{\mathbf{J}} + Q \frac{\frac{3}{2} \hat{\mathbf{I}} \cdot \hat{\mathbf{J}} \left( 2\hat{\mathbf{I}} \cdot \hat{\mathbf{J}} + 1 \right) - \hat{\mathbf{I}}^2 \hat{\mathbf{J}}^2}{2I J (2I - 1) (2J - 1)}, \quad (2)$$

with the electronic total angular momentum  $\hat{\mathbf{J}}$  and the nuclear spin  $\hat{\mathbf{I}}$ , both multiplied by their corresponding magneton ( $\mu_B$  and  $\mu_N$ ) and their g-factor,  $g_J = 3/2$  and  $g_I = -0.67989$ , respectively.[42] The hyperfine constants are  $A = 2\pi \times -1094.361(11)$  MHz and  $Q = 2\pi \times -836.351(79)$  MHz.[43] This gives rise to the Breit-Rabi diagram shown in Fig. 1. For sufficiently large magnetic fields, the splitting between levels in the excited state may exceed several hundred MHz, which enables the proposed scheme for selective state control.

Internal states may be labeled either in the uncoupled basis  $|n, m_J, m_I\rangle$ , where  $n$  denotes the electronic state, e.g.  $^1S_0$  or  $^3P_1$ , and  $m_J$  and  $m_I$  are the projections of electronic and nuclear angular momentum, or in the coupled hyperfine basis  $|n, F, m_F\rangle$ , where  $\mathbf{F} = \mathbf{J} + \mathbf{I}$  is the total angular momentum and  $m_F$  is its projection on the quantization axis. In finite magnetic fields, neither  $F$  nor the separate labels  $m_J$  and  $m_I$  are generally good quantum numbers: the Zeeman term mixes different  $F$  components, while the hyperfine interaction mixes different  $m_J$  and  $m_I$  components. For  $\mathbf{B}$  oriented along the  $z$ -axis, only  $m_F = m_J + m_I$  remains conserved. Since the excited states only serve as an auxiliary tool to enable the transitions between the hyperfine levels of the ground state manifold, the choice of basis is not important, and we use whichever representation is most convenient.

We now introduce the atom–field interaction Hamiltonian for a laser field with electronic Rabi frequency  $\Omega_E$  and polarization angle  $\theta$ . Within the rotating-wave and dipole approximations, this interaction is

$$H_{\text{AF}}(\Omega_E, \theta) = \frac{1}{2} \Omega_E \left( \boldsymbol{\epsilon}(\theta) \cdot \hat{\mathbf{D}} + \text{h.c.} \right) \otimes \mathbb{1}, \quad (3)$$

with the polarization vector  $\boldsymbol{\epsilon}(\theta) = [\sin(\theta), 0, \cos(\theta)]^\top$ , the normalized dipole operator  $\hat{\mathbf{D}} = [\hat{D}_x, \hat{D}_y, \hat{D}_z]^\top$  and with  $\mathbb{1}$  denoting the unit matrix in the nuclear subspace. In the selected basis  $|n, m_J\rangle$  the normalized dipole oper-

ator reads

$$\begin{aligned}\hat{D}_x &= \frac{1}{\sqrt{2}} \left( |^3P_1, -1\rangle \langle ^1S_0, 0| - |^3P_1, +1\rangle \langle ^1S_0, 0| \right), \\ \hat{D}_y &= \frac{i}{\sqrt{2}} \left( |^3P_1, -1\rangle \langle ^1S_0, 0| + |^3P_1, +1\rangle \langle ^1S_0, 0| \right), \\ \hat{D}_z &= |^3P_1, 0\rangle \langle ^1S_0, 0|.\end{aligned}\quad (4)$$

The electronic Rabi frequency  $\Omega_E$  is a measure of the laser intensity. In App. A we provide a more detailed discussion of the relation of these two quantities.

### B. Effective Hyperfine Hamiltonian

We decompose the Hilbert space into a ground-state manifold  $\mathcal{G} = \text{span}\{|^1S_0, m_I\rangle\}$  and an excited-state manifold  $\mathcal{E} = \text{span}\{|^3P_1, m_J, m_I\rangle\}$ , such that the considered Hilbert space is a direct sum  $\mathcal{H} = \mathcal{G} \oplus \mathcal{E}$ . With respect to this decomposition, the Hamiltonian assumes the block structure

$$H(\mathbf{B}, \Delta, \Omega_E, \theta) = \begin{bmatrix} H_{\mathcal{G}}(\mathbf{B}) & W(\Omega_E, \theta) \\ W^\dagger(\Omega_E, \theta) & H_{\mathcal{E}}(\mathbf{B}, \Delta) \end{bmatrix}, \quad (5)$$

where

$$\begin{aligned}H_{\mathcal{G}}(\mathbf{B}) &:= P_{\mathcal{G}} H_Z(\mathbf{B}) P_{\mathcal{G}}, \\ H_{\mathcal{E}}(\mathbf{B}, \Delta) &:= P_{\mathcal{E}} (H_Z(\mathbf{B}) + H_{\text{HF}} - \Delta) P_{\mathcal{E}}, \\ W(\Omega_E, \theta) &:= P_{\mathcal{G}} H_{\text{AF}}(\Omega_E, \theta) P_{\mathcal{E}}\end{aligned}\quad (6)$$

and  $P_{\mathcal{G}}$ ,  $P_{\mathcal{E}}$  denote the projectors onto the ground- and excited-state manifolds, respectively. Likewise, the state vector can be decomposed as

$$|\Psi(t)\rangle = P_{\mathcal{G}} |\Psi(t)\rangle + P_{\mathcal{E}} |\Psi(t)\rangle = |\psi_{\mathcal{G}}(t)\rangle + |\psi_{\mathcal{E}}(t)\rangle. \quad (7)$$

Using the block structure in Eq. (5), the Schrödinger equation  $i\partial_t |\Psi\rangle = H |\Psi\rangle$  yields the coupled equations

$$\begin{aligned}i\partial_t |\psi_{\mathcal{G}}\rangle &= H_{\mathcal{G}} |\psi_{\mathcal{G}}\rangle + W |\psi_{\mathcal{E}}\rangle, \\ i\partial_t |\psi_{\mathcal{E}}\rangle &= H_{\mathcal{E}} |\psi_{\mathcal{E}}\rangle + W^\dagger |\psi_{\mathcal{G}}\rangle.\end{aligned}\quad (8)$$

For suitably chosen detuning  $\Delta$ , the excited manifold  $\mathcal{E}$  is populated only virtually, and one can eliminate it by crudely assuming  $\partial_t |\psi_{\mathcal{E}}\rangle \approx 0$ , which leads to

$$|\psi_{\mathcal{E}}\rangle \approx -H_{\mathcal{E}}^{-1} W^\dagger |\psi_{\mathcal{G}}\rangle. \quad (10)$$

A more rigorous derivation of the effective evolution is provided in App. B or Ref. [44]. Inserting this expression in Eq. (8) gives an effective ground-state evolution, and the effective Hamiltonian

$$i\partial_t |\psi_{\mathcal{G}}\rangle = H_{\text{eff}} |\psi_{\mathcal{G}}\rangle, \quad H_{\text{eff}} = H_{\mathcal{G}} - W H_{\mathcal{E}}^{-1} W^\dagger, \quad (11)$$

which governs the dynamics of the nuclear spin qudit.

By isolating the contribution of the polarization and the electronic Rabi frequency, we can write the effective Hamiltonian more explicitly as

$$H_{\text{eff}}(\mathbf{B}, \Delta, \Omega_E, \theta) = H_{\mathcal{G}}(\mathbf{B}) - \frac{\Omega_E^2}{4} \boldsymbol{\epsilon}^\dagger(\theta) \hat{\alpha}(\mathbf{B}, \Delta) \boldsymbol{\epsilon}(\theta), \quad (12)$$

where  $\hat{\alpha}(\mathbf{B}, \Delta)$  is an operator-valued dynamic polarizability tensor acting on the nuclear-spin manifold, with components

$$\hat{\alpha}_{ij}(\mathbf{B}, \Delta) := P_{\mathcal{G}} (\hat{D}_i^\dagger \otimes \mathbb{1}) H_{\mathcal{E}}(\mathbf{B}, \Delta)^{-1} (\hat{D}_j \otimes \mathbb{1}) P_{\mathcal{G}}. \quad (13)$$

In the nuclear-spin basis  $\{|m_I\rangle\}$ , the effective Hamiltonian is five-diagonal (see App. B 2 for details) and can be written as

$$\begin{aligned}H_{\text{eff}} &= \sum_{m_I} \left[ E_{m_I}^{\mathcal{G}} - \frac{\Omega_E^2}{4} (s_{m_I}^z \cos^2 \theta + s_{m_I}^x \sin^2 \theta) \right] |m_I\rangle \langle m_I| \\ &\quad - \frac{\Omega_E^2}{4} \sum_{m_I} \left[ g_{m_I} \sin \theta \cos \theta |m_I\rangle \langle m_I+1| + \text{h.c.} \right] \\ &\quad - \frac{\Omega_E^2}{4} \sum_{m_I} \left[ h_{m_I} \sin^2 \theta |m_I\rangle \langle m_I+2| + \text{h.c.} \right],\end{aligned}\quad (14)$$

with ground state energies  $E_{m_I}^{\mathcal{G}} = \langle m_I | H_{\mathcal{G}} | m_I \rangle$ , and coefficients given by matrix elements of the polarizability tensor,

$$\begin{aligned}s_{m_I}^z &:= \langle m_I | \hat{\alpha}_{zz} | m_I \rangle, & s_{m_I}^x &:= \langle m_I | \hat{\alpha}_{xx} | m_I \rangle, \\ g_{m_I} &:= \langle m_I | \hat{\alpha}_{xz} + \hat{\alpha}_{zx} | m_I+1 \rangle, & h_{m_I} &:= \langle m_I | \hat{\alpha}_{xx} | m_I+2 \rangle.\end{aligned}\quad (15)$$

In addition to the coherent dynamics, spontaneous decay from the excited manifold  $\mathcal{E}$  induces incoherent scattering. In the regime of predominantly virtual excitation, the scattering rate scales as  $\Gamma_{\text{sc}} \sim \Gamma p_{\mathcal{E}}$ , where  $p_{\mathcal{E}}$  is the excited-state population. Perturbatively,  $p_{\mathcal{E}} \sim \Omega_E^2 / 4\delta_{\text{min}}^2$  with

$$\delta_{\text{min}} = \min_{\nu} |E_{\nu}(\mathbf{B}) + \Delta|, \quad (16)$$

where  $E_{\nu}(\mathbf{B})$  denotes the excited-state eigenenergies at magnetic field  $\mathbf{B}$ . For an operation frequency  $f_{\text{op}} \approx 100$  kHz, the number of scattered photons per operation is bounded by

$$N_{\text{sc}} \leq \Gamma p_{\mathcal{E}} / f_{\text{op}} \lesssim 0.1, \quad (17)$$

when using an excited-state population bound of  $p_{\mathcal{E}} \leq 0.01$ . Below, we therefore use the excited-state population as a feasibility constraint to keep this bound small and neglect incoherent scattering in the analytical discussion of the control scheme.

## IV. UNIVERSAL OPTICAL SINGLE-QUDIT GATES

The effective Hamiltonian in Eq. (14) provides a convenient description of the nuclear-spin dynamics in the ground-state manifold. Its five-diagonal structure naturally separates two types of operations that can be used to realize universal single-qudit control: Raman-induced transitions between neighboring spin states and

state-dependent phase shifts. In the following, we analyze these two mechanisms and determine the parameter regimes in which they can be implemented with high fidelity.

### A. Raman transitions between neighboring states

Raman transitions between neighboring nuclear-spin states  $|m_I\rangle$  and  $|m_I + 1\rangle$  are governed by the diagonal and nearest-neighbor terms of the effective Hamiltonian in Eq. (14). A transition becomes resonant when the light-induced Stark shifts compensate the Zeeman splitting between the two states, while the off-diagonal term proportional to  $g_{m_I}$  sets the Raman coupling. Thus, by tuning the polarization angle  $\theta$  and the laser parameters  $(B, \Delta, \Omega_E)$ , coherent population transfer can be driven selectively between neighboring states.

#### 1. Magic angle

From the effective Hamiltonian in Eq. (14) we obtain the diagonal energies

$$E_{\text{eff}}(m_I) = E_{m_I}^{\mathcal{G}} - \frac{\Omega_E^2}{4} (s_{m_I}^z \cos^2 \theta + s_{m_I}^x \sin^2 \theta),$$

which defines the effective energy difference between neighboring states

$$\delta E_{\text{eff}, m_I} = E_{\text{eff}}(m_I + 1) - E_{\text{eff}}(m_I).$$

Using Eq. (14), this energy difference can be written explicitly as

$$\delta E_{\text{eff}, m_I} = \delta E_{m_I}^{\mathcal{G}} - \frac{\Omega_E^2}{4} [\delta s_{m_I}^z \cos^2 \theta + \delta s_{m_I}^x \sin^2 \theta],$$

where  $\delta E_{m_I}^{\mathcal{G}} = E_{m_I+1}^{\mathcal{G}} - E_{m_I}^{\mathcal{G}}$  denotes the Zeeman splitting of the ground-state manifold, and  $\delta s_{m_I}^{z,x} = s_{m_I+1}^{z,x} - s_{m_I}^{z,x}$ .

A Raman resonance occurs when this effective splitting vanishes. For given parameters  $(B, \Delta, \Omega_E)$ , we therefore define the polarization angle that minimizes the energy difference

$$\theta_{m_I}^*(B, \Delta, \Omega_E) = \arg \min_{\theta \in [0, \pi/2]} |\delta E_{\text{eff}, m_I}|. \quad (18)$$

If the minimum occurs at the boundary,  $\theta \in \{0, \pi/2\}$ , full transitions cannot be driven between neighboring states. However, if the minimum occurs within the interval  $(0, \pi/2)$ , a *magic polarization angle* exists. The two states then become resonant, and coherent transitions can be driven. Solving the resonance condition  $\delta E_{\text{eff}, m_I} = 0$  yields

$$\sin^2 \theta_{m_I}^* = \frac{4 \delta E_{m_I}^{\mathcal{G}} / \Omega_E^2 - \delta s_{m_I}^z}{\delta s_{m_I}^x - \delta s_{m_I}^z}. \quad (19)$$

A *magic angle* therefore exists if and only if the right-hand side lies in the interval  $[0, 1]$ . An illustration is provided in Fig. 2(c), where the intersection of the effective levels indicates the existence of a magic angle for the corresponding transition.

With equal effective energies of  $|m_I\rangle$  and  $|m_I + 1\rangle$ , the corresponding off-diagonal matrix element of the effective Hamiltonian drives coherent population transfer between the states. From Eq. (14) we obtain the mixing matrix element

$$\langle m_I + 1 | H_{\text{eff}} | m_I \rangle = -\frac{\Omega_E^2}{4} g_{m_I} \sin \theta \cos \theta,$$

which determines the rate of the induced transitions. In particular, Rabi oscillations between the states occur with the Raman frequency

$$\Omega_R(m_I) = \frac{\Omega_E^2}{2} |g_{m_I} \sin \theta_{m_I}^* \cos \theta_{m_I}^*|. \quad (20)$$

The existence of a magic angle is a necessary but not sufficient condition for high-fidelity transitions. In addition, the excited-state population must remain small, and unwanted couplings to other levels of the ground state manifold must be suppressed. These conditions determine the feasible regions in parameter space discussed below.

#### 2. Feasibility conditions

In addition to the resonance condition, two further constraints must be satisfied to obtain high-fidelity transitions.

First, the excited-state population must remain small. From the adiabatic-elimination approximation in Eq. (10) one obtains the crude bound

$$p_{\mathcal{E}} := \|\psi_{\mathcal{E}}\|^2 \approx \langle \psi_{\mathcal{G}} | W H_{\mathcal{E}}^{-2} W^\dagger | \psi_{\mathcal{G}} \rangle \leq \frac{\Omega_E^2}{4 \delta_{\min}^2}, \quad (21)$$

where  $\delta_{\min}$  denotes the minimum detuning from the excited-state manifold. Throughout this work, we require

$$p_{\mathcal{E}} \leq 10^{-2}. \quad (22)$$

The dependence of the selected upper bound as a function of  $\delta_{\min}$  is illustrated in Fig. 2(d) for different values of  $\Omega_E$ . The selected threshold is indicated by a dashed horizontal line.

Second, unwanted mixing with other levels of the ground state manifold must remain small. Using the effective Hamiltonian, we estimate the maximum transition probability or ‘loss’ to non-target states  $k$  as

$$L_k \lesssim \frac{\Omega_k^2}{\Omega_k^2 + \delta_k^2}, \quad (23)$$

where  $\Omega_k$  and  $\delta_k$  denote the effective coupling and detuning of the corresponding transition. We impose the requirement

$$L_k \leq 10^{-2}. \quad (24)$$

We define *feasible regions* in parameter space as regions where a) a magic polarization angle exists, b) the excited-state occupation bound is satisfied, and c) the leakage to other ground states remains below the chosen threshold.

### 3. Phase diagram of nearest neighbor transitions

The resulting phase diagram is shown in Fig. 2(a) and (b). Panel (a) presents a scan over magnetic field  $B$  and detuning  $\tilde{\Delta}$ , where we introduce the shifted detuning

$$\tilde{\Delta} = \Delta - \frac{1}{2I+1} \sum_{\nu=1}^{2I+1} E_{\nu}, \quad (25)$$

which centers the excited state levels of the  $m_J = -1$  manifold around zero and improves the visibility of the relevant resonances. The black lines indicate the energies of the excited-state levels of the  $m_J = -1$  manifold (as in a Breit-Rabi diagram), while the colored regions show the corresponding feasible regions for Raman transitions. Each transition is labeled and colored according to the lower nuclear-spin state involved.

When the laser frequency lies close to one of the excited state levels, the polarizability coefficients entering the effective Hamiltonian vary strongly, leading to large differential light shifts. In the regions between two such resonances, the light shifts can compensate the Zeeman splitting of a pair of neighboring ground states, which allows the resonance condition  $\delta E_{\text{eff}, m_I} = 0$  to be satisfied for a suitable polarization angle. As a result, feasible regions for Raman transitions appear in the intervals between adjacent excited-state levels.

The detailed shape of these regions is governed by two competing effects. On the one hand, approaching an excited-state resonance increases the magnitude of the light shifts, which facilitates the cancellation of the ground-state splitting and therefore favors the existence of a magic angle. On the other hand, the population of the excited manifold grows as the detuning decreases, which restricts how close the laser frequency can be placed to the resonance. Consequently, the feasible regions are bounded on both sides by the condition that the excited-state occupation remains below the chosen threshold.

The dependence on the magnetic field arises from the changing structure of the excited-state eigenvectors. At moderate magnetic fields, the hyperfine interaction mixes electronic and nuclear degrees of freedom, so that the excited states contain significant admixtures of different  $m_I$  components. This mixing enables the laser-induced light shifts to couple neighboring nuclear-spin

states in the ground manifold. As the magnetic field increases further, the eigenstates approach the Paschen-Back regime, where the nuclear and electronic degrees of freedom become approximately decoupled. In this limit, the admixture between different nuclear-spin projections is reduced, the differential light shifts become smaller, and the feasible regions for Raman transitions gradually shrink. Eventually, the required light shifts cannot be generated without violating the excited-state population constraint, and coherent transitions are no longer accessible.

The  $\Delta$ - $\Omega_E$  slices shown in Fig. 2(b) further illustrate the structure of the feasible regions. The left boundary is determined by the magic-angle condition: if  $\Omega_E$  is too small, the light shifts are insufficient to compensate for the ground-state splitting. The upper and lower boundaries arise from the excited-state population constraint, which requires larger detuning as the laser intensity increases. The right boundary, when present, is determined by the mixing condition. At sufficiently large laser intensities, off-resonant couplings to other ground states become significant, leading to unwanted mixing and leakage from the target transition. Despite appearing narrow for some transitions on the scale of the plotted parameter range, the feasible regions still provide sufficient freedom to adjust both the laser detuning and intensity to reliably access the desired operating points.

The achievable Raman Rabi frequencies  $\Omega_R(m_I)$  within the feasible regions are indicated by the color scale. At intermediate magnetic fields, the increasing separation of the excited-state levels allows the laser to be placed farther from resonance while still generating sufficiently strong differential light shifts. Larger laser intensities can therefore be used without violating the excited-state population constraint, and since the Raman coupling scales as  $\Omega_R \propto \Omega_E^2$ , this directly leads to higher transition rates. At larger fields, however, the excited-state eigenvectors gradually approach the Paschen-Back regime and the admixture between different nuclear-spin projections decreases. Consequently, increasingly large light shifts are required to compensate the ground-state splitting, while the excited-state population constraint limits the usable laser intensity. This combination leads to a plateau and eventual reduction of the achievable Raman transition strengths.

Fig. 2(e) summarizes these results as a function of magnetic field. The gray curve indicates the minimum electronic Rabi frequency required for the existence of a magic angle. To provide a robust graphical summary, we characterize each transition by the median and maximum Raman Rabi frequency within its feasible region. The shaded region in Fig. 2(e) spans the median, over all transitions, of these two quantities. It therefore indicates a typical operating range rather than an absolute bound.

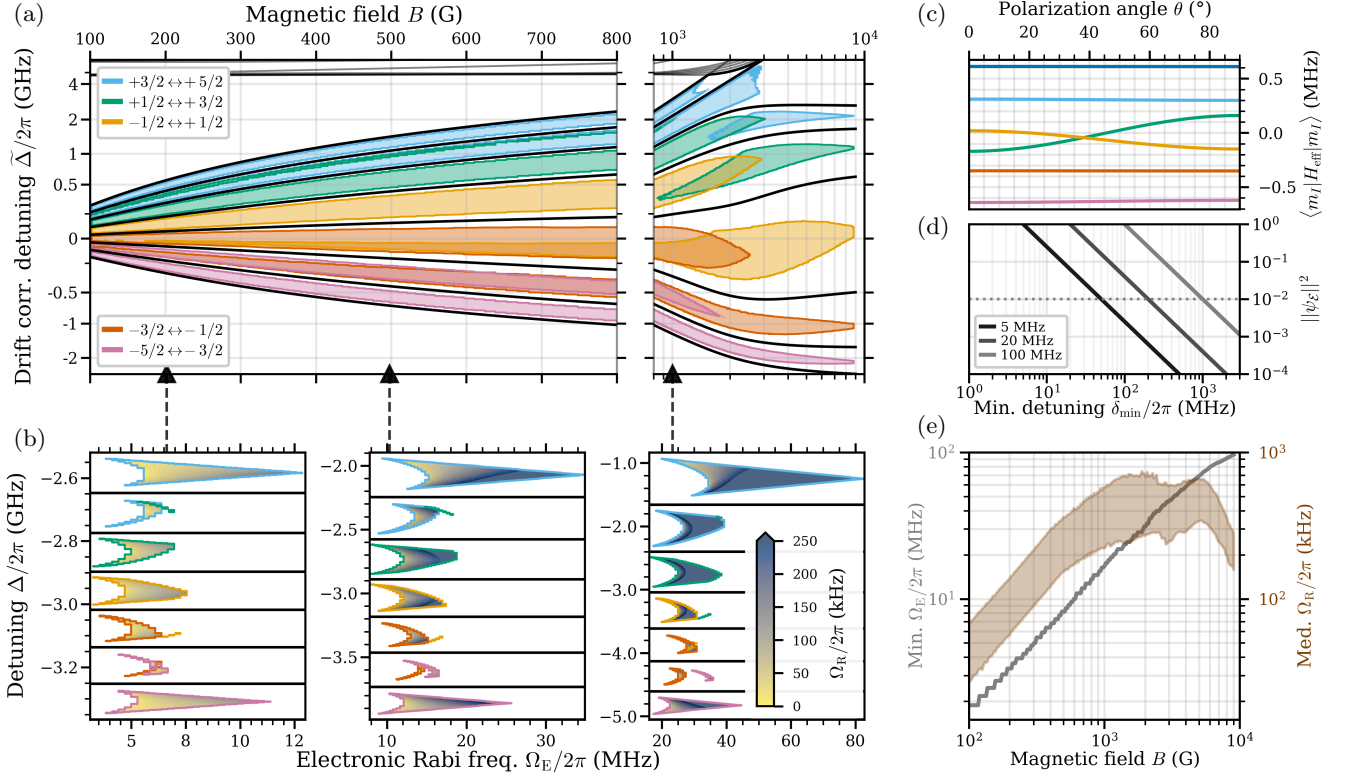


FIG. 2: Phase diagram of Raman transitions between neighboring nuclear-spin states. (a) Feasible regions for Raman transitions in the  $B$ - $\tilde{\Delta}$  plane. Black lines indicate the energies of the excited-state levels, while colored regions denote feasible parameter regimes for the corresponding transitions, labeled by the lower nuclear-spin state. (b)  $\Delta$ - $\Omega_E$  slices at selected magnetic fields illustrating the structure of the feasible regions; the color scale indicates the achievable Raman Rabi frequency  $\Omega_R$ . (c) Example of the effective energy difference  $\delta E_{\text{eff}, m_I}$  at  $B = 500$  G,  $\Delta = -3$  GHz,  $\Omega_E = 15$  MHz as a function of the polarization angle  $\theta$ , showing the crossing of the  $m_I = -1/2$  and  $m_I = +1/2$  levels that defines the magic angle. (d) Upper bound on the excited-state population as a function of the minimum detuning  $\delta_{\text{min}}$  for several electronic Rabi frequencies  $\Omega_E \in \{5 \text{ MHz}, 20 \text{ MHz}, 100 \text{ MHz}\}$ , illustrating the characteristic  $1/\delta_{\text{min}}^2$  scaling. (e) Summary of achievable Raman transition strengths versus magnetic field. The gray curve indicates the minimum electronic Rabi frequency required for the existence of a magic angle, while the shaded region represents the typical range of achievable Raman Rabi frequencies across all transitions, obtained from the median of the transition medians within the feasible regions and the median of the corresponding maxima.

## B. Phase gates via state-dependent light-shifts

Similarly, we analyze the structure of phase operations generated by state-dependent light shifts. For phase gates, we choose a polarization angle  $\theta = 0$ , for which the effective Hamiltonian in Eq. (14) becomes purely diagonal. In this configuration, no transitions between different nuclear-spin states are driven, and the laser field induces only level-dependent energy shifts. The effective Hamiltonian reduces to

$$H_{\text{eff}}(\theta=0) = \sum_{m_I} \left( E_{m_I}^G - \frac{\Omega_E^2}{4} s_{m_I}^z(B, \Delta) \right) |m_I\rangle \langle m_I|, \quad (26)$$

such that the additional light shift of level  $|m_I\rangle$ , centered around the mean shift of the ground-state manifold, is

given by

$$S_{m_I} = -\frac{\Omega_E^2}{4} \left( s_{m_I}^z(B, \Delta) - \frac{1}{2I+1} \sum_{m'_I} s_{m'_I}^z(B, \Delta) \right). \quad (27)$$

The phase accumulation rates are therefore set by the  $zz$  component  $s_{m_I}^z$  of the polarizability tensor. The maximal achievable centered light shifts are shown in Fig. 3(a-c), where for each detuning we choose the largest electronic Rabi frequency  $\Omega_E$  compatible with the population constraint  $p_E \leq 0.01$ . Thick lines indicate the levels accumulating the largest phase shifts, while the upper panels show the corresponding maximal values of  $\Omega_E$ . Thus, all light-shift values below the indicated thick curves can be realized by suitably adjusting the electronic Rabi frequency.

Panels (a-c) illustrate the resulting light-shift struc-

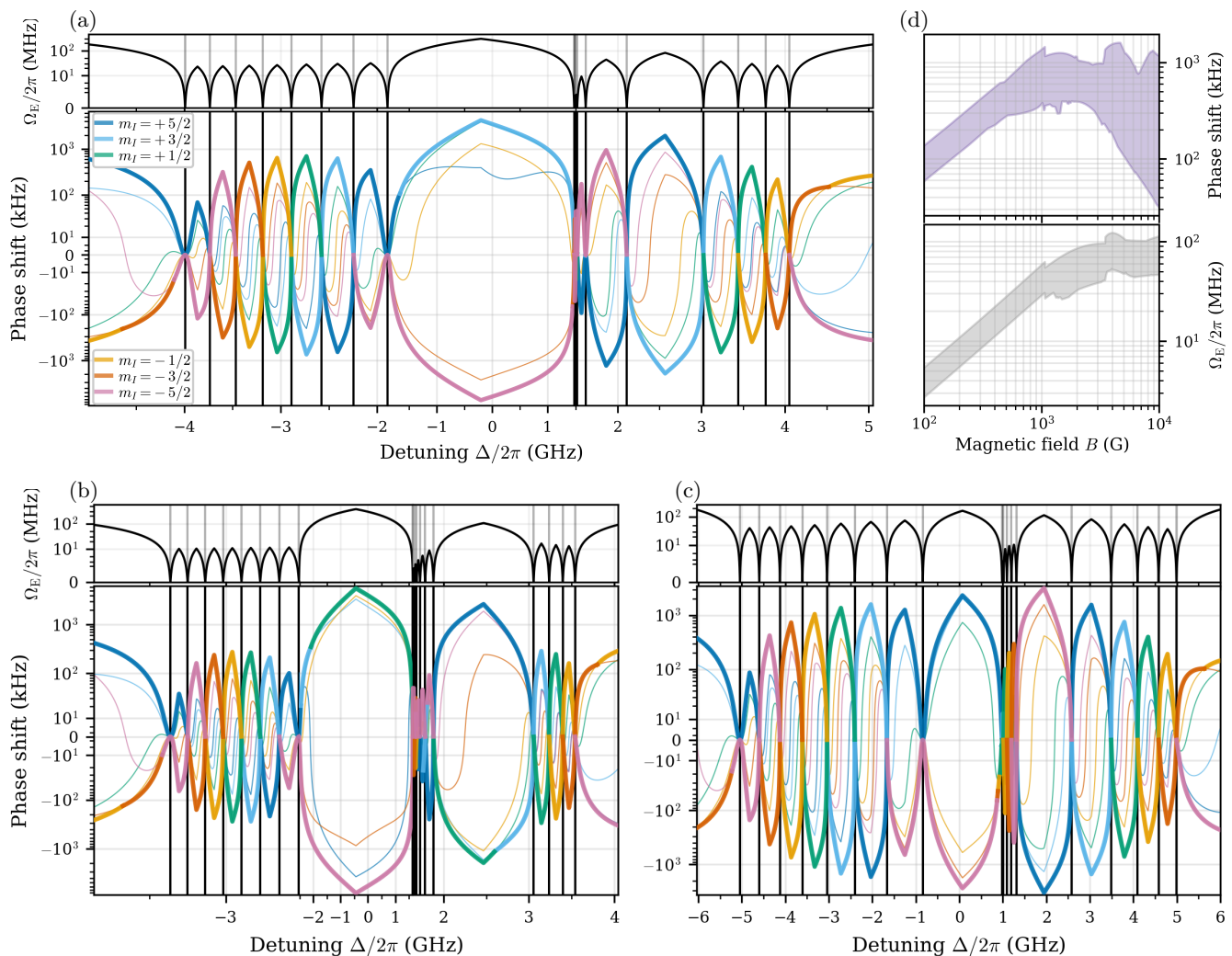


FIG. 3: Structure of phase gates generated by state-dependent light shifts for  $\theta = 0$ . (a–c) Maximal achievable centered light shifts  $S_{m_I}$  as a function of detuning  $\Delta$  for magnetic fields  $B = 500$  G (a),  $200$  G (b), and  $1000$  G (c). For each detuning, the electronic Rabi frequency  $\Omega_E$  is chosen as large as possible while satisfying the excited-state population constraint  $p_E \leq 0.01$ . Thick lines indicate the dominant levels accumulating the largest phase shifts, while the upper panels show the corresponding maximal values of  $\Omega_E$ . (d) Summary of achievable phase accumulation rates versus magnetic field. The shaded region indicates a representative range across all levels, computed from the median of the level medians and the median of the corresponding maxima, while the lower panel shows the corresponding electronic Rabi frequencies.

ture as a function of  $\Delta$  for magnetic fields of  $B = 500$  G,  $200$  G, and  $1000$  G, respectively. We focus on  $B = 500$  G as a representative operating point for the subsequent discussion, as it provides a good compromise between experimental feasibility and achievable gate speeds. As in the case of Raman transitions, different nuclear-spin states become dominant depending on the laser detuning, reflecting the admixture of nuclear-spin components in the eigenstates of the excited-state manifold. By appropriately choosing the laser frequency, each level can be made dominant in the sense that it accumulates the largest phase shift.

The characteristic shape of the curves can be under-

stood from the scaling of the light shift and the excited-state population. The light shift scales as  $\Omega_E^2/\delta_{\min}$ , whereas the excited-state occupation scales as  $\Omega_E^2/\delta_{\min}^2$ . Since the maximal allowed electronic Rabi frequency is determined by the population constraint  $p_E \leq 0.01$ , the largest achievable shifts occur at detunings that are sufficiently far from the excited-state resonances, where larger laser intensities can be applied while remaining within the population bound.

Comparing panels (a–c) shows how the accessible phase shifts depend on magnetic field. The smaller excited-state level spacing at  $200$  G restricts the usable detuning range, while the larger spacing at  $1000$  G al-

lows higher laser intensities before the excited-state population bound is reached. For improved visibility, the central region between the  $m_J = -1$  and  $m_J = 0$  manifolds is compressed in the figure.

As can be inferred from the figure, phase accumulation rates exceeding 100 kHz are readily achievable for each level. Furthermore, the light shifts typically appear in pairs of opposite sign: one level experiences a strong positive phase shift while another acquires a similarly large negative phase. Consequently, the dominant effect is a large relative phase accumulation between two levels, determined by the admixture of nuclear-spin components in the excited-state manifold.

Fig. 3(d) provides a representative graphical summary of the achievable phase accumulation rates over a range of magnetic fields. For each level, we compute the median and maximum achievable phase shifts over the feasible detuning range; the shaded region is then defined by the median of the level medians and the median of the level maxima. It therefore indicates a typical operating range rather than a strict bound. The lower panel shows the corresponding electronic Rabi frequencies obtained using the same procedure.

The overall magnetic-field dependence can be understood from the interplay of level spacing and excited-state mixing. At moderate magnetic fields, the increasing separation of the excited-state levels allows larger laser intensities to be used while remaining sufficiently detuned, which leads to faster phase accumulation. At larger magnetic fields, the excited states gradually approach the Paschen–Back regime and the admixture of  $m_J = 0$  components decreases. Since for  $\theta = 0$  only the  $m_J = 0$  manifold contributes significantly to the light shifts, this reduction of mixing limits the achievable phase shifts and leads to the observed plateau and eventual decrease of the phase accumulation rate. This limitation could, in principle, be circumvented by using  $\theta = 90^\circ$  or circularly polarized light, which would allow the  $m_J = \pm 1$  manifolds to contribute to the light shifts. However, for magnetic fields below approximately 1000 G, the  $\theta = 0$  configuration already provides sufficiently strong and spectrally clean phase shifts, and we therefore do not pursue these alternatives further.

Overall, phase accumulation rates exceeding 100 kHz are readily achievable at 500 G, comparable to the speeds of the Raman flip operations discussed above.

### C. Universality of single-qudit control

The flip and phase operations discussed above are sufficient for universal single-qudit control on the six-dimensional nuclear-spin manifold. In Lie-algebraic terms, the available Hamiltonians generate  $\mathfrak{su}(d)$  up to a global phase, allowing arbitrary unitary operations on the qudit to be synthesized. This follows from the fact that nearest-neighbor couplings, together with a nontrivial diagonal Hamiltonian, form a sufficient generating set

for  $\mathfrak{su}(d)$  [2, 12].

In our scheme, both ingredients arise directly from the effective Hamiltonian in Eq. (14). For  $\theta = \theta_{m_I}^*$ , the Hamiltonian realizes a resonant and dominant flip between neighboring states  $|m_I\rangle$  and  $|m_I + 1\rangle$ , while retaining diagonal light shifts on all levels and, in general, weak next-nearest-neighbor couplings proportional to  $h_{m_I}$ . For  $\theta = 0$ , the off-diagonal terms in Eq. (14) vanish, and the Hamiltonian reduces to the purely diagonal form in Eq. (26), which generates state-dependent phase shifts on all levels. Thus, the available controls form a family of five-diagonal Hamiltonians with dominant nearest-neighbor couplings and additional residual terms, yet still generate  $\mathfrak{su}(d)$ . The phase operation provides selectivity, while the neighboring couplings ensure connectivity across the manifold. A detailed proof is given in App. C.

Importantly, a single nontrivial diagonal phase operation is already sufficient for universality. In the present scheme, however, the detuning dependence of the light shifts yields a continuous family of diagonal phase profiles, offering additional flexibility and substantially reducing the overhead of compiled gate sequences in practice.

## V. TWO-QUDIT GATES VIA RYDBERG INTERACTION

Entangling operations in neutral-atom quantum processors are commonly performed by exciting selected computational states to highly excited Rydberg levels. When two nearby atoms are simultaneously excited, the strong Rydberg–Rydberg interaction shifts the doubly excited state out of resonance if the interaction energy exceeds the excitation Rabi frequency. This effect is commonly referred to as the Rydberg blockade mechanism and can be used to realize CZ gates [19]. In combination with the universal single-qudit control developed above, such an entangling operation enables universal qudit computation [40]. In the following, we discuss which Rydberg states of  $^{173}\text{Yb}$  are suitable for such gates.

Ytterbium is alkaline-earth-like and effectively has two valence electrons. As a result, a single Rydberg series is typically composed of multiple channels, each attached to different ionization thresholds. These channels can interact and may require a multichannel quantum defect theory (MQDT) treatment [45]. While the Rydberg level structures of  $^{171}\text{Yb}$  and  $^{174}\text{Yb}$  have been studied extensively [46, 47], the  $^{173}\text{Yb}$  isotope considered in this manuscript is less established. Since  $^{173}\text{Yb}$  has nuclear spin  $I = 5/2$ , the MQDT model structure differs from that of  $^{171}\text{Yb}$  ( $I = 1/2$ ), and these models cannot be transferred directly. A useful exception is the  $6sns^3S_1$ ,  $F = 7/2$  series, where the dominant channel is attached to a single ionization threshold, namely  $6s_{1/2}F_c = 3$ , and therefore largely avoids channel interactions. Consequently, the  $6sns^3S_1$ ,  $F = 7/2$  series should be de-

scribed, to good approximation, by the MQDT model of the bosonic  $^{174}\text{Yb}$   $6sns^3S_1$  series [48, 49]. This approximation has been applied with high accuracy to the analogous  $6sns^3S_1$ ,  $F = 3/2$  series in  $^{171}\text{Yb}$  [46]. Note that this simplification does not hold for the  $6sns$ ,  $F = 5/2$  series in  $^{173}\text{Yb}$ , which consists of channels attached to the hyperfine-split ionization thresholds  $6s_{1/2}F_c = 2$  and  $6s_{1/2}F_c = 3$ , giving rise to strong inter-channel mixing.

We therefore focus on Rydberg states belonging to the  $6sns^3S_1$ ,  $F = 7/2$  series. Their suitability for entangling gates is governed by the associated pair-state interaction shifts. At the few-micrometer separations, typical of tweezer arrays, these interactions are predominantly of van der Waals type and depend sensitively on nearby opposite-parity  $6snp$  pair states, whose spectrum is not yet sufficiently characterized for  $^{173}\text{Yb}$ . In  $^{171}\text{Yb}$ , however, Rydberg states from the analogous  $6sns^3S_1$ ,  $F = 3/2$  series have recently been used to realize fast, high-fidelity CZ gates at magnetic fields as large as 500 G [25]. This operating regime is compatible with the magnetic fields required for the single-qudit gates proposed here (see Sec. IV), suggesting that similar entangling operations should be achievable for  $^{173}\text{Yb}$ .

For the Rydberg excitation, the addressed pair state is conveniently chosen from the two stretched states  $|6sns^3S_1, F = 7/2, m_F = \pm 7/2\rangle$ . The choice should match the sign of the van der Waals coefficient  $C_6$ . For repulsive interactions ( $C_6 > 0$ ), the Zeeman-split manifold of  $|6sns^3S_1, 7/2, m_F\rangle$  pair states bends toward higher energies. Hence, the lower stretched pair state with  $m_F = -7/2$  remains spectrally cleaner, while the upper stretched pair state with  $m_F = +7/2$  can encounter resonances with other  $m_F$  combinations. For attractive interactions ( $C_6 < 0$ ), the situation is reversed, and the upper stretched state is preferable. We therefore propose a two-photon excitation scheme [25] that addresses the appropriate stretched computational state. Starting from  $|^1S_0, F = 5/2, m_F = \pm 5/2\rangle$ , circularly polarized light drives the stretched transition to  $|^3P_1, F = 7/2, m_F = \pm 7/2\rangle$ , using  $\sigma_+$  light for  $m_F = +5/2$  and  $\sigma_-$  light for  $m_F = -5/2$ . Because these stretched states are the unique extremal states of the corresponding  $m_F$  manifolds, they remain unmixed eigenstates of the Zeeman–hyperfine Hamiltonian considered here. Their Clebsch–Gordan coefficients are maximal, which maximizes the optical coupling for a given laser power. A second,  $\pi$ -polarized laser then couples the intermediate state to the target Rydberg state  $|6sns^3S_1, F = 7/2, m_F = \pm 7/2\rangle$ . Such an excitation scheme can be combined with state-of-the-art optimal-control protocols [50, 51] to realize high-fidelity and fast ( $\mu\text{s}$  timescale) CZ gates [25].

## VI. STATE-SELECTIVE READOUT

State-selective readout is realized via optical cycling transitions that distinguish a single “bright” state from

the remaining “dark” states of the ground-state manifold. In the present system, such a scheme can be implemented using either the narrow  $^3P_1$  transition or the broad  $^1P_1$  transition. The same stretched-state structure also underlies the Rydberg excitation scheme discussed in Sec. V.

In both cases, a stretched ground state  $|^1S_0, F = 5/2, m_F = \pm 5/2\rangle$  is coupled to a corresponding stretched excited state  $|n, F = 7/2, m_F = \pm 7/2\rangle$ , with  $n \in \{^3P_1, ^1P_1\}$ , forming a closed cycling transition. At the level of the Zeeman–hyperfine Hamiltonians considered here, these stretched states remain unmixed eigenstates for any magnetic field, because they are the unique extremal states of the corresponding  $m_F$  manifolds. Their corresponding Clebsch–Gordan coefficients are therefore maximal. The addressed state acts as the bright state and undergoes repeated photon scattering, while all other ground states are off-resonantly coupled and therefore remain dark. In principle, either stretched transition can be used. At larger magnetic fields, however, nearby excited-state crossings make the more isolated stretched state preferable, and we focus on that choice below.

Because of the different hyperfine structure of the two excited-state manifolds, the optimal choice of stretched state differs. For the  $^3P_1$  manifold (see Fig. 1), the level structure favors a well-isolated cycling transition for the lower stretched state  $|^3P_1, F = 7/2, m_F = -7/2\rangle$ , equivalently  $|^3P_1, m_J = -1, m_I = -5/2\rangle$ . In contrast, the  $^1P_1$  manifold exhibits a different level ordering due to the dominant quadrupole interaction, and the upper stretched state  $|^1P_1, F = 7/2, m_F = +7/2\rangle$ , equivalently  $|^1P_1, m_J = +1, m_I = +5/2\rangle$ , provides the most robust and spectrally isolated transition. A detailed discussion of the  $^1P_1$  structure is given in App. D.

Despite these differences, the underlying readout mechanism is identical: a single bright state is resonantly driven, while all other states remain off-resonant. A detailed model is provided in App. E. The relevant quantities are the bright-state scattering rate  $R_B$ , the dark-state scattering rate  $R_D$ , and the contrast  $C := R_B/R_D$ .

The resulting performance is shown in Fig. 4. The left panels display the bright-state scattering rate  $R_B$ , while the right panels show the contrast  $C$  as a function of magnetic field  $B$  and driving strength  $\Omega_E$ . Contour lines indicate the normalized dark-state scattering rate  $R_D/\Gamma$ , providing a direct measure of leakage from the dark manifold.

A clear tradeoff between speed and selectivity is observed. The  $^3P_1$  transition, with its narrow linewidth  $\Gamma_{3P_1} = 2\pi \times 183 \text{ kHz}$ , [24, 41] strongly suppresses off-resonant excitation and yields extremely low dark-state scattering rates, resulting in very high contrast. However, the achievable scattering rate  $R_B$  is limited by the small decay rate, leading to comparatively slow readout.

In contrast, the  $^1P_1$  transition, with linewidth  $\Gamma_{1P_1} = 2\pi \times 29.1 \text{ MHz}$ , [52] enables scattering rates that are orders of magnitude larger, allowing for fast readout. At

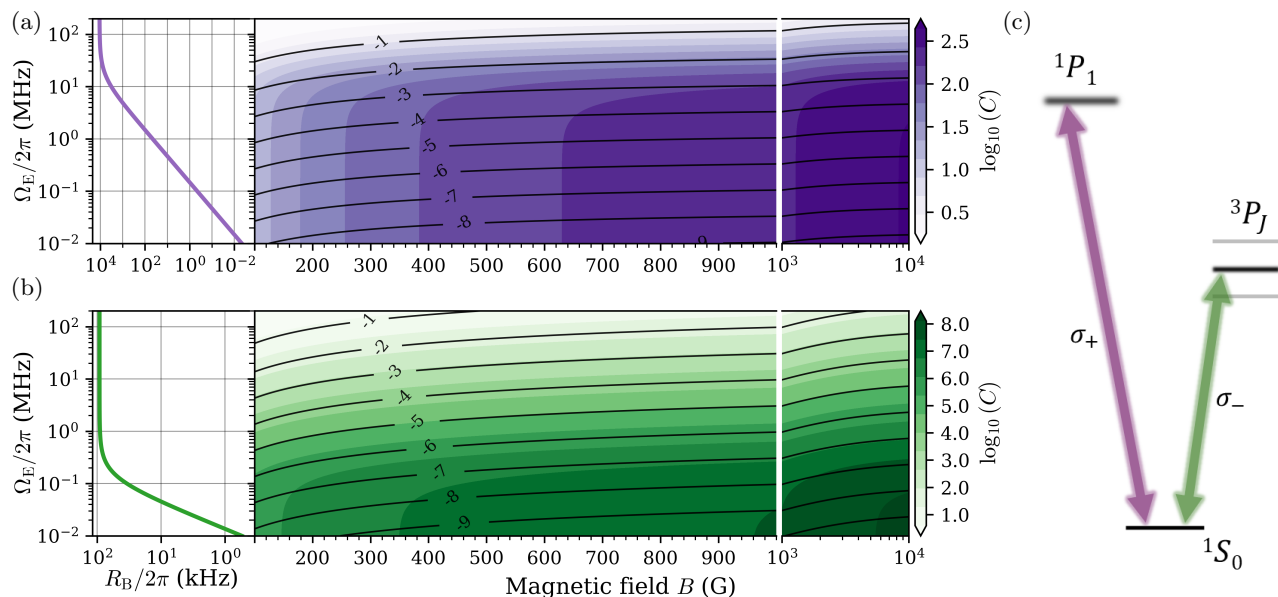


FIG. 4: Readout performance for the  $^3P_1$  and  $^1P_1$  transitions. (a)  $^3P_1$  bright-state scattering rate  $R_B$  (left) and contrast  $C$  (right) as a function of magnetic field and driving strength. (b) Same as (a) for the  $^1P_1$  transition. Contour lines in the contrast plots indicate the normalized dark-state scattering rate  $R_D/\Gamma$ . (c) Schematic illustration of the readout scheme. The purple  $\sigma_+$  path addresses the upper stretched  $^1S_0 \rightarrow ^1P_1$  cycling transition, while the green  $\sigma_-$  path addresses the lower stretched  $^1S_0 \rightarrow ^3P_1$  cycling transition.

the same time, the broader linewidth reduces spectral selectivity, leading to increased off-resonant excitation and lower, but still substantial, contrast. The larger decay rate also requires higher driving strengths to reach comparable saturation, although this is facilitated by the larger dipole matrix element (see App. A).

Typical operating regimes illustrate this behavior: for the  $^1P_1$  transition, we find  $R_D/\Gamma \sim 10^{-3}$  and  $C \sim 10^2$ , with bright-state scattering rates exceeding 1 MHz. In contrast, the  $^3P_1$  transition achieves  $R_D/\Gamma \lesssim 10^{-5}$  and  $C \gtrsim 10^5$ , with  $R_B$  bounded by  $\sim 10^2$  kHz, corresponding to near-ideal state discrimination. Note that in both cases the contrast can be slightly improved at the cost of reduced readout speed by introducing a small detuning of the readout beam from the stretched state resonance.

Overall, the two transitions provide complementary readout regimes:  $^3P_1$  enables highly selective detection at lower speed, while  $^1P_1$  allows fast readout at reduced contrast.

## VII. CONCLUSION AND OUTLOOK

In this work, we demonstrated that fast and selective universal single-qudit control in  $^{173}\text{Yb}$  can be achieved using single-beam Raman transitions in moderate magnetic fields. The regime between 500 and 1000 G provides an optimal balance between hyperfine-induced state mixing and spectral selectivity, enabling gate frequencies exceeding 100 kHz. The central control mechanism

is the existence of a magic polarization angle  $\theta_{m_I}^*$ , at which neighboring nuclear-spin states become resonant while off-resonant couplings remain suppressed. Together with state-dependent phase shifts, these nearest-neighbor Raman transitions generate universal control of the six-dimensional ground-state manifold.

Rydberg-mediated interactions provide a natural route toward two-qudit gates. While stretched-state implementations can build directly on existing Rydberg-blockade schemes, extending such gates to the full qudit manifold in moderate to high magnetic fields remains an open challenge. In this regime, the usual description in terms of good hyperfine quantum numbers  $F$  and  $m_F$  breaks down, and the level structure is governed by the interplay of fine structure, hyperfine coupling, and Zeeman interaction. Early studies of Rydberg atoms in strong magnetic fields demonstrate that such regimes remain in principle tractable [53–56], and recent experiments in ytterbium have confirmed the feasibility of Rydberg blockade at several hundred Gauss [27]. At the same time, quantitative modeling of Yb Rydberg states requires detailed, experimentally validated approaches [46], indicating that further spectroscopic and theoretical work will be necessary to enable high-fidelity two-qudit gates in  $^{173}\text{Yb}$  in moderate to high magnetic fields.

State-selective readout can be implemented via stretched-state cycling transitions. The narrow  $^3P_1$  transition enables high-contrast detection at limited scattering rates, while the broad  $^1P_1$  transition allows for fast readout at reduced contrast, defining a flexible

tradeoff between speed and selectivity. Large magnetic fields are furthermore compatible with standard cooling schemes and can even enable spin-resolved or coherence-preserving cooling mechanisms [57, 58].

From a control-theoretic perspective, the rich internal structure of neutral atoms enables highly selective operations, but also requires precise control within complex multi-level manifolds. In this setting, optimal-control methods provide a natural framework for pulse engineering and have been successfully applied to multi-level and open quantum systems.[59, 60] In the present case, however, multiple optical drives introduce distinct rotating frames and thus different effective Hamiltonians, such that standard fixed-Hamiltonian formulations are not directly applicable. Extending optimal-control techniques to such multi-frequency, multi-level dynamics, therefore, represents an important direction for future work.

Overall, these results identify neutral  $^{173}\text{Yb}$  as a promising platform for rapid and robust all-optical hyperfine-qudit control. Its combination of a multi-level nuclear-spin ground-state manifold and large excited-state hyperfine splittings enables fast, state-selective single-qudit operations, while stretched-state Rydberg excitation and optical cycling provide compatible routes toward entangling gates and readout.

### Appendix A: Conversion between Rabi frequency and laser intensity

For the proposed protocol, the electronic Rabi frequency  $\Omega_E/2\pi$  of the  $(6s^2) ^1S_0 \rightarrow (6s6p) ^3P_1$  transition in  $^{173}\text{Yb}$  serves as a convenient measure of the required laser intensity. The relation between electronic Rabi frequency and laser intensity is set by the unnormalized dipole matrix element of the transition,

$$\mathcal{D} = \left| \langle ^1S_0 | \hat{\mathbf{d}} | ^3P_1 \rangle \right| = \frac{0.54(8)}{\sqrt{3}} \text{ a.u.},$$

together with a Wigner factor of  $1/\sqrt{3}$  [61].

The link between the laser intensity  $\mathcal{I}$  and the Rabi frequency follows from

$$\hbar\Omega_E = -\langle ^1S_0 | \hat{\mathbf{d}} | ^3P_1 \rangle \cdot \mathbf{E}_0,$$

where the electric field amplitude  $\mathbf{E}_0$  is related to the intensity via  $\mathcal{I} = \frac{1}{2}\epsilon_0 c E_0^2$ . Combining these expressions yields

$$|\hbar\Omega_E| = \mathcal{D} \sqrt{\frac{2\mathcal{I}}{\epsilon_0 c}}. \quad (\text{A1})$$

Using this formula, electronic Rabi frequencies of  $\Omega_E/2\pi = 10, 20, 40$  MHz correspond to intensities of  $\mathcal{I} = 0.02, 0.08, 0.3$  W/cm<sup>2</sup>, respectively. For a Gaussian beam with waist  $w_0$ , the peak intensity is  $\mathcal{I} = \frac{2P}{\pi w_0^2}$ , where  $P$  denotes the optical power. Hence, these intensities map to optical powers of a few microwatts for beam diameters in the range 20–100  $\mu\text{m}$ .

This analysis demonstrates that electronic Rabi frequencies in the MHz range can be achieved with only tens of microwatts of optical power, well within the capabilities of current neutral-atom tweezer and optical lattice experiments.

### Appendix B: Adiabatic Elimination and Five-Diagonal Structure

In this appendix, we derive the effective Hamiltonian in Eq. (12) from the block form in Eq. (5) following the adiabatic-elimination procedure [44], and we establish the five-diagonal structure in Eq. (14) in the nuclear-spin basis.

#### 1. Adiabatic elimination in the $\mathcal{H} = \mathcal{G} \oplus \mathcal{E}$ decomposition

Beyond the crude condition  $\partial_t |\psi_{\mathcal{E}}\rangle \approx 0$ , we can derive the effective Hamiltonian rigorously. Following Ref. [44], we integrate the evolution equation of the excited state in Eq. (9) to obtain

$$|\psi_{\mathcal{E}}(t)\rangle = e^{-iH_{\mathcal{E}}t} |\psi_{\mathcal{E}}(0)\rangle - i \int_0^t e^{-iH_{\mathcal{E}}(t-\tau)} W^\dagger |\psi_{\mathcal{G}}(\tau)\rangle d\tau.$$

Inserting this expression into Eq. (8) yields an *exact* integro-differential equation for  $|\psi_{\mathcal{G}}\rangle$ ,

$$i \partial_t |\psi_{\mathcal{G}}(t)\rangle = H_{\mathcal{G}} |\psi_{\mathcal{G}}(t)\rangle - i \int_0^t W e^{-iH_{\mathcal{E}}(t-\tau)} W^\dagger |\psi_{\mathcal{G}}(\tau)\rangle d\tau, \quad (\text{B1})$$

where we assumed that the excited manifold is initially unpopulated,  $|\psi_{\mathcal{E}}(0)\rangle = 0$ . Furthermore, assuming that the detuning is sufficiently large such that  $|\psi_{\mathcal{G}}(t)\rangle$  varies slowly on the timescale set by  $H_{\mathcal{E}}$ , one may perform a zeroth-order Markov approximation and replace  $|\psi_{\mathcal{G}}(\tau)\rangle \approx |\psi_{\mathcal{G}}(t)\rangle$  under the integral; this separation of timescales is enhanced by choosing the energy origin at the center of gravity of the ground-state manifold, as discussed in Ref. [44]. With the substitution  $s = t - \tau$ , Eq. (B1) becomes local in time,

$$i \partial_t |\psi_{\mathcal{G}}(t)\rangle = \left( H_{\mathcal{G}} - \Sigma(t) \right) |\psi_{\mathcal{G}}(t)\rangle \quad (\text{B2})$$

with  $\Sigma(t) := i \int_0^t W e^{-iH_{\mathcal{E}}s} W^\dagger ds$ .

The time-dependent self-energy  $\Sigma(t)$  can be evaluated exactly,

$$\Sigma(t) = W \left( H_{\mathcal{E}}^{-1} [1 - e^{-iH_{\mathcal{E}}t}] \right) W^\dagger \approx W H_{\mathcal{E}}^{-1} W^\dagger,$$

where the last approximation follows by averaging the oscillating part since  $e^{-iH_{\mathcal{E}}t}$  oscillates rapidly on a timescale  $\sim 1/|\Delta|$  as the spectrum of  $H_{\mathcal{E}}$  is set by the optical detuning  $\Delta$  (up to Zeeman and hyperfine splittings). Together, this yields the effective Hamiltonian in Eq. (11).

## 2. Five-diagonal effective Hamiltonian

We show that  $\langle m | H_{\text{eff}} | m' \rangle = 0$  for  $|m - m'| > 2$ . Since  $H_{\mathcal{G}}$  is diagonal in  $|^1S_0, m_I\rangle$ , it suffices to analyze the second-order term  $WH_{\mathcal{E}}^{-1}W^\dagger$ . First, the dipole operators act only on electronic degrees of freedom and therefore preserve the nuclear projection. Hence any change  $m' \rightarrow m$  must occur within the excited-manifold resolvent  $H_{\mathcal{E}}^{-1}$ . Second, in the excited manifold, we work in the basis  $|^3P_1, m_J, m_I\rangle$  with  $m_J \in \{-1, 0, +1\}$ . The only terms capable of changing  $m_I$  are those containing nuclear ladder operators. In particular, the hyperfine interaction contains  $I_{\pm}J_{\mp}$ , which changes  $(m_I, m_J)$  as

$$\begin{aligned} I_+J_- &: (m_J, m_I) \mapsto (m_J - 1, m_I + 1), \\ I_-J_+ &: (m_J, m_I) \mapsto (m_J + 1, m_I - 1). \end{aligned}$$

Because  $m_J$  is restricted to three values, repeated application of  $J_{\pm}$  can change  $m_J$  by at most two units. Therefore, along any sequence of hyperfine-induced couplings inside  $\mathcal{E}$ , the nuclear projection can change by at most two units,  $|m_I - m'_I| \leq 2$ . Since  $D_i^\dagger$  again preserves  $m_I$ , the full second-order operator satisfies  $\langle m | (D_i^\dagger \otimes \mathbb{1}) H_{\mathcal{E}}^{-1} (D_j \otimes \mathbb{1}) | m' \rangle = 0$  for  $|m - m'| > 2$ , which proves that  $H_{\text{eff}}$  is five-diagonal in the  $\{|m_I\rangle\}$  basis.

The coefficient sequences  $s_m^{x,z}$ ,  $g_m$ , and  $h_m$  used in Eq. (14) follow directly from the corresponding matrix elements of  $\hat{\alpha}_{ij}$  as defined in Eq. (15).

### Appendix C: Proof of universal single-qudit controllability

To show that the generated set of Hamiltonians is universal, we consider the effective Hamiltonian in Eq. (14) and the corresponding control operations discussed in the main text. The key idea is that diagonal phase operations provide selectivity between transitions, while the neighboring couplings connect all states.

#### 1. Available control Hamiltonians

Let  $\{|j\rangle\}_{j=1}^d$  denote the ordered nuclear-spin basis. The effective Hamiltonian in Eq. (14) can be written as

$$H_{\text{eff}} = D + \sum_{j=1}^{d-1} a_j X_j^{(1)} + \sum_{j=1}^{d-2} b_j X_j^{(2)}, \quad (\text{C1})$$

with diagonal  $D$ , nearest-neighbor couplings

$$X_j^{(1)} := |j\rangle\langle j+1| + |j+1\rangle\langle j|, \quad (\text{C2})$$

and, in general, next-nearest-neighbor terms

$$X_j^{(2)} := |j\rangle\langle j+2| + |j+2\rangle\langle j|. \quad (\text{C3})$$

For suitable control parameters with magic angle  $\theta = \theta_j^*$ , the coefficient  $a_j$  of the targeted neighboring transition

is nonzero and dominant. For  $\theta = 0$ , the Hamiltonian becomes diagonal and generates phase operations

$$H_\phi = \sum_{j=1}^d \lambda_j |j\rangle\langle j|. \quad (\text{C4})$$

To keep the proof simple, we assume that one available phase Hamiltonian  $H_\phi$  has the property that the neighboring level differences

$$\Delta_j := \lambda_j - \lambda_{j+1}, \quad j = 1, \dots, d-1, \quad (\text{C5})$$

are pairwise distinct and nonzero. Since the scheme provides a continuous family of diagonal phase profiles through the detuning dependence of the light shifts, such a generic choice is always possible, except near isolated accidental degeneracies. Still, in any case, several phase gates can be added to the control set, restoring or enhancing controllability.

#### 2. Isolation of individual neighboring couplings

We define the antisymmetric operators

$$\begin{aligned} Y_j^{(1)} &:= -i(|j\rangle\langle j+1| - |j+1\rangle\langle j|), \\ Y_j^{(2)} &:= -i(|j\rangle\langle j+2| - |j+2\rangle\langle j|). \end{aligned} \quad (\text{C6})$$

A direct calculation gives, for  $k = 1, 2$ ,

$$[H_\phi, X_j^{(k)}] = i(\lambda_j - \lambda_{j+k}) Y_j^{(k)}, \quad (\text{C7})$$

and therefore

$$[H_\phi, [H_\phi, X_j^{(k)}]] = (\lambda_j - \lambda_{j+k})^2 X_j^{(k)}. \quad (\text{C8})$$

Thus, the double commutator with  $H_\phi$  acts diagonally on the off-diagonal couplings. In particular, we also have  $[H_\phi, [H_\phi, D]] = 0$  for every diagonal operator  $D$ , as  $[H_\phi, D] = 0$ .

Fixing one targeted flip Hamiltonian  $H_j^{\text{flip}} = H_{\text{eff}}$  generated at a magic angle  $\theta_j^*$ , we consider the linear map

$$\mathcal{L}(A) := [H_\phi, [H_\phi, A]]. \quad (\text{C9})$$

By the relations above,  $\mathcal{L}$  satisfies

$$\begin{aligned} \mathcal{L}(D) &= 0, \\ \mathcal{L}(X_k^{(1)}) &= (\lambda_k - \lambda_{k+1})^2 X_k^{(1)}, \\ \mathcal{L}(X_k^{(2)}) &= (\lambda_k - \lambda_{k+2})^2 X_k^{(2)}. \end{aligned} \quad (\text{C10})$$

Hence  $\mathcal{L}$  multiplies each off-diagonal coupling by a scalar depending on the corresponding level difference.

Because the numbers  $\Delta_k^2$  are distinct, there exists a polynomial  $p_j$  such that

$$p_j(0) = 0, \quad p_j(\Delta_j^2) = 1, \quad p_j(\Delta_k^2) = 0 \quad (k \neq j), \quad (\text{C11})$$

and, if desired, also  $p_j((\lambda_k - \lambda_{k+2})^2) = 0$  for all next-nearest-neighbor terms present in  $H_j^{\text{flip}}$  whose eigenvalues are nonzero or non-negligible. An explicit choice is obtained by Lagrange interpolation over the finite set of conditions given above.

Applying this polynomial to  $H_j^{\text{flip}}$  gives

$$p_j(\mathcal{L}) H_j^{\text{flip}} = a_j X_j^{(1)}. \quad (\text{C12})$$

Thus, the pure nearest-neighbor generator  $X_j^{(1)}$  is obtained from the full five-diagonal Hamiltonian. Commuting once with  $H_\phi$  then yields

$$[H_\phi, X_j^{(1)}] = i\Delta_j Y_j^{(1)}, \quad (\text{C13})$$

so  $Y_j^{(1)}$  is also generated. Therefore, for every neighboring pair, the available controls generate both  $X_j^{(1)}$  and  $Y_j^{(1)}$ .

### 3. Generation of $\mathfrak{su}(d)$

From  $X_j^{(1)}$  and  $Y_j^{(1)}$  one obtains the diagonal difference

$$Z_j := |j\rangle\langle j| - |j+1\rangle\langle j+1| \quad (\text{C14})$$

through the commutator  $[X_j^{(1)}, Y_j^{(1)}] = 2i Z_j$ . Hence, for each neighboring pair, the generators  $X_j^{(1)}$ ,  $Y_j^{(1)}$ ,  $Z_j$  span the full local  $\mathfrak{su}(2)$  algebra.

Since generators exist for all neighboring pairs, the system forms a connected chain. Starting from adjacent generators, longer-range couplings are generated by commutators of overlapping pairs. For example, one obtains operators of the form

$$X_j^{(2)} \propto [X_j^{(1)}, Y_{j+1}^{(1)}], \quad (\text{C15})$$

and similarly for larger separations by iterating this construction along the chain.

Using the same argument as above, each such coupling yields the corresponding  $Y$  and  $Z$  operators, so that a full  $\mathfrak{su}(2)$  algebra is generated on every pair of levels  $(j, k)$ . Since the chain is connected, this implies that all pairs of levels are coupled, and therefore the full  $\mathfrak{su}(d)$  algebra is generated.

### Appendix D: The $^1P_1$ state of $^{173}\text{Yb}$

The readout scheme discussed in Sec. VI of the main text can also be implemented using the  $(6s^2) ^1S_0 \rightarrow (6s6p) ^1P_1$  transition in  $^{173}\text{Yb}$ , which is centered around a transition frequency of  $\omega_0$  corresponding to 399 nm.[41] The Hamiltonian takes the same form as in Eq. (1), with identical Zeeman, hyperfine, and atom-field interaction terms, but with parameters corresponding to the  $^1P_1$  manifold.

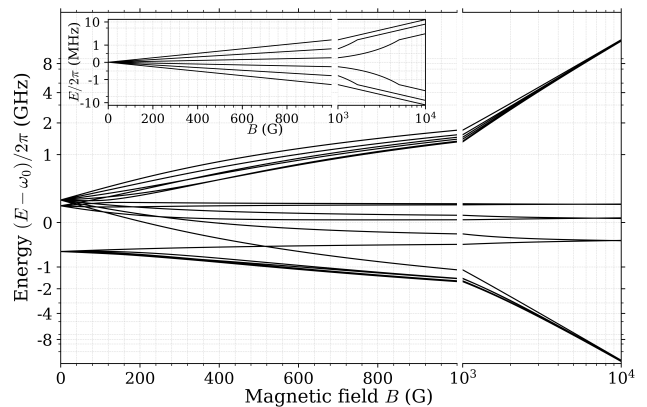


FIG. 5: Breit-Rabi diagram of the  $^1P_1$  state in  $^{173}\text{Yb}$ . The main plot illustrates the magnetic-field-dependent level structure of the  $^1P_1$  manifold, while the inset displays the ground-state manifold; both plots are suitably scaled to enhance visibility.

In contrast to the  $^3P_1$  state, the  $^1P_1$  state exhibits a much larger decay rate,  $\Gamma = 2\pi \times 29$  MHz,[52] which implies a significantly larger dipole matrix element,[61]

$$\mathcal{D} = \left| \langle ^1S_0 | \hat{d} | ^1P_1 \rangle \right| = \frac{4.4(8)}{\sqrt{3}} \text{ a.u.},$$

and consequently allows for substantially larger achievable electronic Rabi frequencies  $\Omega_E$  (see App. A).

The hyperfine structure of the  $^1P_1$  state is dominated by the electric quadrupole interaction, with  $Q = 2\pi \times 610.47(84)$  MHz and a comparatively small magnetic dipole constant  $A = 2\pi \times 57.91(12)$  MHz.[62] The resulting level structure is shown in Fig. 5.

In contrast to the  $^3P_1$  manifold, the strong quadrupole interaction and the different signs of the hyperfine constants lead to a qualitatively different ordering of the hyperfine levels. As a consequence, the upper stretched state  $|^1P_1, m_J = +1, m_I = +5/2\rangle$  provides the most isolated and robust cycling transition for state-selective readout.

### Appendix E: General readout model

To describe the readout approach, we employ an effective two-level model applicable to both the  $^3P_1$  and  $^1P_1$  transitions, where a stretched-state cycling transition defines the bright state and all other states are off-resonantly coupled. At the level of the Zeeman-hyperfine Hamiltonians considered here, the addressed stretched states are unique extremal states and remain unmixed eigenstates. This gives maximal Clebsch-Gordan coefficients, making the cycling transition efficient in terms of laser power.

The scattering dynamics of the bright state are then

described by an effective two-level scattering rate

$$R_B(\delta) = \frac{\Gamma}{2} \frac{s}{1 + s + (2\delta/\Gamma)^2}, \quad s = \frac{2\Omega_E^2}{\Gamma^2}, \quad (\text{E1})$$

where  $\delta$  is the detuning from the transition,  $\Gamma$  is the decay rate from the excited-state manifold to the ground state, and  $s$  is the saturation parameter. On resonance, this approaches the saturation limit  $R_B \rightarrow \Gamma/2$ , which sets the maximal readout speed.

All other ground states are detuned from the addressed transition. Their scattering rates can therefore be bounded by treating each possible transition as an independent two-level system. For a state  $|k\rangle$  with detuning  $\delta_k$  and coupling strength  $\Omega_k$ , one obtains the upper bound

$$R_k \leq \frac{\Gamma}{2} \frac{s_k}{1 + s_k + (2\delta_k/\Gamma)^2}, \quad s_k = \frac{2\Omega_k^2}{\Gamma^2}, \quad (\text{E2})$$

with detuning  $\delta_k$ , and the effective Rabi frequency  $\Omega_k =$

$\beta_k \Omega_E$ , with  $\beta_k$  denoting the relative coupling strength of the transition. The dominant dark-state scattering rate is then defined as  $R_D = \max_k R_k$ , which is typically set by the closest unwanted transition.

The readout performance is characterized by the contrast

$$C = \frac{R_B}{R_D}, \quad (\text{E3})$$

together with the absolute scale of  $R_B$ , which determines the readout speed.

## ACKNOWLEDGMENTS

We acknowledge funding by the Austrian Science Fund (FWF) [10.55776/P36903]. We further thank the IT Services (ZID) of the Graz University of Technology for providing high-performance computing resources and technical support.

- 
- [1] Y. Wang, Z. Hu, B. C. Sanders, and S. Kais, Qudits and high-dimensional quantum computing, *Frontiers in Physics* **Volume 8 - 2020**, 10.3389/fphy.2020.589504 (2020).
- [2] M. Luo and X. Wang, Universal quantum computation with qudits, *Sci. China Phys. Mech. Astron.* **57**, 1712 (2014).
- [3] Z. Jia, W. Huie, L. Li, W. K. C. Sun, X. Hu, Aakash, H. Kogan, A. Karve, J. Y. Lee, and J. P. Covey, An architecture for two-qubit encoding in neutral ytterbium-171 atoms, *npj Quantum Information* **10**, 106 (2024).
- [4] D. González-Cuadra, T. V. Zache, J. Carrasco, B. Kraus, and P. Zoller, Hardware efficient quantum simulation of non-abelian gauge theories with qudits on rydberg platforms, *Phys. Rev. Lett.* **129**, 160501 (2022).
- [5] T. V. Zache, D. González-Cuadra, and P. Zoller, Fermion-qudit quantum processors for simulating lattice gauge theories with matter, *Quantum* **7**, 1140 (2023).
- [6] M. Ringbauer, M. Meth, L. Postler, R. Stricker, R. Blatt, P. Schindler, and T. Monz, A universal qudit quantum processor with trapped ions, *Nat. Phys.* , 1053 (2022).
- [7] M. Meth, J. Zhang, J. F. Haase, C. Edmunds, L. Postler, A. J. Jena, A. Steiner, L. Dellantonio, R. Blatt, P. Zoller, T. Monz, P. Schindler, C. Muschik, and M. Ringbauer, Simulating two-dimensional lattice gauge theories on a qudit quantum computer, *Nature Physics* **21**, 570 (2025).
- [8] E. T. Campbell, Enhanced fault-tolerant quantum computing in  $d$ -level systems, *Phys. Rev. Lett.* **113**, 230501 (2014).
- [9] S. Omanakuttan, A. Mitra, M. J. Martin, and I. H. Deutsch, Quantum optimal control of ten-level nuclear spin qudits in  $^{87}\text{Sr}$ , *Phys. Rev. A* **104**, L060401 (2021).
- [10] S. Omanakuttan, A. Mitra, E. J. Meier, M. J. Martin, and I. H. Deutsch, Qudit entanglers using quantum optimal control, *PRX Quantum* **4**, 040333 (2023).
- [11] J. K. Krondorfer, M. Diez, and A. W. Hauser, Single-qudit control in  $^{87}\text{Sr}$  via optical nuclear electric resonance, *Phys. Rev. A* **112**, 062614 (2025).
- [12] G. K. Brennen, D. P. O’Leary, and S. S. Bullock, Criteria for exact qudit universality, *Phys. Rev. A* **71**, 052318 (2005).
- [13] H. Ahmed, A. Litvinov, P. Guesdon, E. Maréchal, J. Huckans, B. Pasquiou, B. Laburthe-Tolra, and M. Robert-de Saint-Vincent, Coherent control over the high-dimensional space of the nuclear spin of alkaline-earth atoms, *PRX Quantum* **6**, 020352 (2025).
- [14] Y. Chi, J. Huang, Z. Zhang, J. Mao, Z. Zhou, X. Chen, C. Zhai, J. Bao, T. Dai, H. Yuan, *et al.*, A programmable qudit-based quantum processor, *Nat. Commun.* **13**, 1166 (2022).
- [15] M. J. Peterer, S. J. Bader, X. Jin, F. Yan, A. Kamal, T. J. Gudmundsen, P. J. Leek, T. P. Orlando, W. D. Oliver, and S. Gustavsson, Coherence and decay of higher energy levels of a superconducting transmon qubit, *Phys. Rev. Lett.* **114**, 010501 (2015).
- [16] E. Svetitsky, H. Suchowski, R. Resh, Y. Shalibo, N. Katz, Y. Rofe, H. Bluhm, D. Mahalu, and A. Frydman, Hidden two-qubit dynamics of a four-level josephson circuit, *Nature Communications* **5**, 5617 (2014).
- [17] J. Randall, S. Weidt, E. D. Standing, K. Lake, S. C. Webster, D. F. Murgia, T. Navickas, K. Roth, and W. K. Hensinger, Efficient preparation and detection of microwave dressed-state qubits and qutrits with trapped ions, *Phys. Rev. A* **91**, 012322 (2015).
- [18] M. M. Boyd, T. Zelevinsky, A. D. Ludlow, S. Blatt, T. Zanon-Willette, S. M. Foreman, and J. Ye, Nuclear spin effects in optical lattice clocks, *Phys. Rev. A* **76**, 022510 (2007).
- [19] M. Saffman, Quantum computing with atomic qubits and rydberg interactions: progress and challenges, *J. Phys. B: At. Mol. Opt. Phys.* **49**, 202001 (2016).
- [20] L. Henriot, L. Beguin, A. Signoles, T. Lahaye, A. Browaeys, G.-O. Reymond, and C. Jurczak, Quantum computing with neutral atoms, *Quantum* **4**, 327 (2020).

- [21] J. W. Lis, A. Senoo, W. F. McGrew, F. Rönchen, A. Jenkins, and A. M. Kaufman, Midcircuit operations using the omg architecture in neutral atom arrays, *Phys. Rev. X* **13**, 041035 (2023).
- [22] N. Chen, L. Li, W. Huie, M. Zhao, I. Vetter, C. H. Greene, and J. P. Covey, Analyzing the rydberg-based optical-metastable-ground architecture for  $^{171}\text{Yb}$  nuclear spins, *Phys. Rev. A* **105**, 052438 (2022).
- [23] S. Ma, A. P. Burgers, G. Liu, J. Wilson, B. Zhang, and J. D. Thompson, Universal gate operations on nuclear spin qubits in an optical tweezer array of  $^{171}\text{Yb}$  atoms, *Phys. Rev. X* **12**, 021028 (2022).
- [24] A. Jenkins, J. W. Lis, A. Senoo, W. F. McGrew, and A. M. Kaufman, Ytterbium nuclear-spin qubits in an optical tweezer array, *Phys. Rev. X* **12**, 021027 (2022).
- [25] J. Muniz, M. Stone, D. Stack, M. Jaffe, J. Kindem, L. Wadleigh, E. Zaly-Geller, X. Zhang, C.-A. Chen, M. Norcia, *et al.*, High-fidelity universal gates in the 171 yb ground-state nuclear-spin qubit, *PRX Quantum* **6**, 020334 (2025).
- [26] S. Ma, G. Liu, P. Peng, B. Zhang, S. Jandura, J. Claes, A. P. Burgers, G. Pupillo, S. Puri, and J. D. Thompson, High-fidelity gates and mid-circuit erasure conversion in an atomic qubit, *Nature* **622**, 279 (2023).
- [27] M. A. Norcia, W. B. Cairncross, K. Barnes, P. Battaglino, A. Brown, M. O. Brown, K. Cassella, C.-A. Chen, R. Coxe, D. Crow, J. Epstein, C. Griger, A. M. W. Jones, H. Kim, J. M. Kindem, J. King, S. S. Kondov, K. Kotru, J. Lauigan, M. Li, M. Lu, E. Megidish, J. Marjanovic, M. McDonald, T. Mittiga, J. A. Muniz, S. Narayanaswami, C. Nishiguchi, R. Notermans, T. Paule, K. A. Pawlak, L. S. Peng, A. Ryou, A. Smull, D. Stack, M. Stone, A. Sucich, M. Urbaneck, R. J. M. van de Veerdonk, Z. Vendeiro, T. Wilkason, T.-Y. Wu, X. Xie, X. Zhang, and B. J. Bloom, Midcircuit qubit measurement and rearrangement in a  $^{171}\text{Yb}$  atomic array, *Phys. Rev. X* **13**, 041034 (2023).
- [28] W. Huie, L. Li, N. Chen, X. Hu, Z. Jia, W. K. C. Sun, and J. P. Covey, Repetitive readout and real-time control of nuclear spin qubits in  $^{171}\text{Yb}$  atoms, *PRX Quantum* **4**, 030337 (2023).
- [29] K. Barnes, P. Battaglino, B. J. Bloom, K. Cassella, R. Coxe, N. Crisosto, J. P. King, S. S. Kondov, K. Kotru, S. C. Larsen, J. Lauigan, B. J. Lester, M. McDonald, E. Megidish, S. Narayanaswami, C. Nishiguchi, R. Notermans, L. S. Peng, A. Ryou, T.-Y. Wu, and M. Yarwood, Assembly and coherent control of a register of nuclear spin qubits, *Nat. Commun.* **13**, 2779 (2022).
- [30] J. K. Krondorfer and A. W. Hauser, Nuclear electric resonance for spatially resolved spin control via pulsed optical excitation in the UV-visible spectrum, *Phys. Rev. A* **108**, 053110 (2023).
- [31] J. K. Krondorfer, M. Diez, and A. W. Hauser, Optical nuclear electric resonance in LiNa: selective addressing of nuclear spins through pulsed lasers, *Phys. Scr.* **99**, 075307 (2024).
- [32] J. K. Krondorfer, S. Pucher, M. Diez, S. Blatt, and A. W. Hauser, Optical nuclear electric resonance as single qubit gate for trapped neutral atoms, *Journal of Physics B: Atomic, Molecular and Optical Physics* **58**, 235001 (2025).
- [33] S. Taie, R. Yamazaki, S. Sugawa, and Y. Takahashi, An  $\text{su}(6)$  mott insulator of an atomic fermi gas realized by large-spin pomeranchuk cooling, *Nature Physics* **8**, 825 (2012).
- [34] F. Scazza, C. Hofrichter, M. Höfer, P. C. De Groot, I. Bloch, and S. Fölling, Observation of two-orbital spin-exchange interactions with ultracold  $\text{su}(n)$ -symmetric fermions, *Nature Physics* **10**, 779 (2014).
- [35] M. A. Cazalilla, A. F. Ho, and M. Ueda, Ultracold gases of ytterbium: ferromagnetism and mott states in an  $\text{su}(6)$  fermi system, *New Journal of Physics* **11**, 103033 (2009).
- [36] D. Xiao, J. Li, W. C. Campbell, T. Dellaert, P. McMillin, A. Ransford, C. Roman, and A. Derevianko, Hyperfine structure of  $^{173}\text{Yb}^+$ : Toward resolving the  $^{173}\text{Yb}$  nuclear-octupole-moment puzzle, *Phys. Rev. A* **102**, 022810 (2020).
- [37] O. Abdel Karim, A. Muzi Falconi, R. Panza, W. Liu, and F. Scazza, Single-atom imaging of  $^{173}\text{yb}$  in optical tweezers loaded by a five-beam magneto-optical trap, *Quantum Science and Technology* **10**, 045019 (2025).
- [38] C. W. Hoyt, Z. W. Barber, C. W. Oates, T. M. Fortier, S. A. Diddams, and L. Hollberg, Observation and absolute frequency measurements of the  $^1s_0-^3p_0$  optical clock transition in neutral ytterbium, *Phys. Rev. Lett.* **95**, 083003 (2005).
- [39] O. Abdel Karim, A. Muzi Falconi, R. Panza, W. Liu, and F. Scazza, Single-atom imaging of  $^{173}\text{yb}$  in optical tweezers loaded by a five-beam magneto-optical trap, *Quantum Science and Technology* **10**, 045019 (2025).
- [40] J.-L. Brylinski and R. Brylinski, Universal quantum gates, in *Mathematics of Quantum Computation*, edited by R. Brylinski and G. Chen (Chapman & Hall/CRC, Boca Raton, FL, 2002) pp. 101–116.
- [41] T. Kuwamoto, K. Honda, Y. Takahashi, and T. Yabuzaki, Magneto-optical trapping of yb atoms using an intercombination transition, *Phys. Rev. A* **60**, R745 (1999).
- [42] N. Stone, Table of nuclear magnetic dipole and electric quadrupole moments, *Atomic Data and Nuclear Data Tables* **90**, 75 (2005).
- [43] P. E. Atkinson, J. S. Schelfhout, and J. J. McFerran, Hyperfine constants and line separations for the  $1s_0-3p_1$  intercombination line in neutral ytterbium with sub-doppler resolution, *Physical Review A* **100**, 10.1103/physreva.100.042505 (2019).
- [44] V. Paulisch, H. Rui, H. K. Ng, and B.-G. Englert, Beyond adiabatic elimination: A hierarchy of approximations for multi-photon processes, *The European Physical Journal Plus* **129**, 12 (2014).
- [45] M. Aymar, C. H. Greene, and E. Luc-Koenig, Multichannel rydberg spectroscopy of complex atoms, *Reviews of Modern Physics* **68**, 1015 (1996).
- [46] M. Peper, Y. Li, D. Y. Knapp, M. Bileska, S. Ma, G. Liu, P. Peng, B. Zhang, S. P. Horvath, A. P. Burgers, and J. D. Thompson, Spectroscopy and modeling of  $^{171}\text{Yb}$  rydberg states for high-fidelity two-qubit gates, *Phys. Rev. X* **15**, 011009 (2025).
- [47] R. Kuroda, V. M. Hughes, M. Poitrinal, M. Peper, and J. D. Thompson, Microwave spectroscopy and multichannel quantum defect analysis of ytterbium 6 snp, 6 snf, and 6 sng rydberg states, *Physical Review A* **112**, 042817 (2025).
- [48] F. Robicheaux, D. Booth, and M. Saffman, Theory of long-range interactions for rydberg states attached to hyperfine-split cores, *Physical Review A* **97**, 022508 (2018).

- [49] F. Hummel, S. Weber, J. Mögerle, H. Menke, J. King, B. Bloom, S. Hofferberth, and M. Li, Engineering rydberg-pair interactions in divalent atoms with hyperfine-split ionization thresholds, *Physical Review A* **110**, 042821 (2024).
- [50] H. Levine, A. Keesling, G. Semeghini, A. Omran, T. T. Wang, S. Ebadi, H. Bernien, M. Greiner, V. Vuletić, H. Pichler, *et al.*, Parallel implementation of high-fidelity multiqubit gates with neutral atoms, *Physical review letters* **123**, 170503 (2019).
- [51] S. Jandura and G. Pupillo, Time-optimal two-and three-qubit gates for rydberg atoms, *Quantum* **6**, 712 (2022).
- [52] H. Letellier, Á. Mitchell Galvão de Melo, A. Dorne, and R. Kaiser, Loading of a large yb mot on the  $1s_0 \rightarrow 1p_1$  transition, *Review of Scientific Instruments* **94**, 123203 (2023).
- [53] W. R. S. Garton, F. S. Tomkins, and H. M. Crosswhite, Magnetic effects in ba i and sr i absorption spectra, *Proceedings of the Royal Society of London. Series A, Mathematical and Physical Sciences* **373**, 189 (1980).
- [54] J. Neukammer, H. Rinneberg, and U. Majewski, Diamagnetic shift and singlet–triplet mixing of yb rydberg states with large radial extent, *Phys. Rev. A* **30**, 1142 (1984).
- [55] T. Pohl, H. R. Sadeghpour, and P. Schmelcher, Cold and ultracold rydberg atoms in strong magnetic fields, *Physics Reports* **484**, 181 (2009).
- [56] F. Robicheaux, Angular dependence of the interaction between two rydberg atoms, *Phys. Rev. A* **97**, 022508 (2018).
- [57] I. Reichenbach and I. H. Deutsch, Sideband cooling while preserving coherences in the nuclear spin state in group-ii-like atoms, *Phys. Rev. Lett.* **99**, 123001 (2007).
- [58] X.-F. Shi, Coherence-preserving cooling of nuclear-spin qubits in a weak magnetic field, *Phys. Rev. A* **107**, 023102 (2023).
- [59] S. J. Glaser, U. Boscain, T. Calarco, C. P. Koch, W. Köckenberger, R. Kosloff, I. Kuprov, B. Luy, S. Schirmer, T. Schulte-Herbrüggen, D. Sugny, and F. K. Wilhelm, Training Schrödinger’s cat: quantum optimal control, *The European Physical Journal D* **69**, 279 (2015).
- [60] C. P. Koch, U. Boscain, T. Calarco, G. Dirr, S. Filipp, S. J. Glaser, R. Kosloff, S. Montangero, T. Schulte-Herbrüggen, D. Sugny, and F. K. Wilhelm, Quantum optimal control in quantum technologies. strategic report on current status, visions and goals for research in Europe, *EPJ Quantum Technology* **9**, 19 (2022).
- [61] S. G. Porsev, Y. G. Rakhлина, and M. G. Kozlov, Electric-dipole amplitudes, lifetimes, and polarizabilities of the low-lying levels of atomic ytterbium, *Phys. Rev. A* **60**, 2781 (1999).
- [62] A. Banerjee, U. D. Rapol, D. Das, A. Krishna, and V. Natarajan, Precise measurements of uv atomic lines: Hyperfine structure and isotope shifts in the 398.8 nm line of yb, *Europhysics Letters* **63**, 340 (2003).